Volcanic cloud detection using Sentinel-3 satellite data by means of neural networks: the Raikoke 2019 eruption test case

Ilaria Petracca[1], Davide De Santis[1], Matteo Picchiani[2,3], Stefano Corradini[4], Lorenzo Guerrieri[4], Fred Prata[5], Luca Merucci[4], Dario Stelitano[4], Fabio Del Frate[1], Giorgia Salvucci[1] and Giovanni Schiavon[1]

[1] Department of Civil Engineering and Computer Science Engineering, Tor Vergata University of Rome, 00133, Italy
[2] GEO-K s.r.l., Rome, Italy
[3] GMATICS s.r.l., Rome, Italy
[4] Istituto Nazionale di Geofisica e Vulcanologia, ONT, 00143 Rome, Italy
[5] AIRES Pty Ltd., Australia

Correspondence to: Ilaria Petracca (ilaria.petracca@uniroma2.it)

Codice campo modificato

Abstract

The accurate automatic volcanic cloud detection by means of satellite data is a challenging task and of great concern for both scientific community and aviation stakeholder due to the well-known issues generated by ~~a~~ strong eruption events in relation to aviation safety and health impacts. In this context, machine learning techniques applied to satellite data acquired from recent spaceborne sensors ~~acquired data~~ have shown promising results in the last years.

This work focuses on the application of a neural network based model to Sentinel-3 SLSTR (Sea and Land Surface Temperature Radiometer) daytime products in order to detect volcanic ash plumes generated by the 2019 Raikoke eruption. A~~The~~ classification of meteorological ~~the~~ clouds and of ~~the~~ other surfaces comprising~~composing~~ the scene is also carried out. The neural network has been trained with MODIS (MODerate resolution Imaging Spectroradiometer) daytime imagery collected during the 2010 Eyjafjallajökull eruption. The similar acquisition channels of SLSTR and MODIS sensors and the ~~events~~ comparable latitudes of the eruptions allow to extend ~~foster the robustness of~~ the approach to SLSTR, ~~which~~thereby overcoming the lack in Sentinel-3~~SLSTR~~ products collected in previous mid-high latitude eruptions. The results show that the neural network model is able to detect volcanic ash with good accuracy if compared with RGB visual inspection and BTD (Brightness Temperature Difference) procedures. Moreover, the comparison between the ash cloud obtained by the neural network (NN) and a plume mask manually generated for the specific SLSTR considered images, shows significant agreement.~~.~~ Thus, the proposed approach allows an automatic image classification during eruption events, and~~which it~~ it is also considerably faster than time-consuming manual~~ly~~ algorithms ~~(e.g. find the best BTD product-specific threshold)~~. Furthermore, the whole image classification indicates an overall reliability of the algorithm, in particular for ~~meteo-clouds~~ recognition and discrimination from volcanic clouds.

~~Finally, the results show that the NN developed for the SLSTR nadir view is able to properly classify also the SLSTR oblique view images.~~

1 Introduction

F~~In general, f~~rom the start of an eruptive event~~the eruption~~, volcanic emissions are composed of a broad distribution of ash particles, ranging from very fine ash (particle diameters, d < 30 µm) increasing in size to tephra (airborne pyroclastic material) with diameters from 2 mm up to 64 mm. Larger fragments are~~and are~~ also generated which fall out quickly; these and ash with d > 30 µm are not considered in this paper. The~~In general, from the start of the eruption, the volcanic emission is composed by both coarse and fine particles. The coarser fall down to the volcanic edifice, while the finer are transported by the wind. The solid part of the volcanic plume is basically composed by ash particles while the~~ gaseous part is made mainly of water vapour (H_2O), carbon dioxide (CO_2) and sulphur dioxide (SO_2) gases ~~(Shinohara, 2008)~~(Oppenheimer et al., 2011; Shinohara, 2008)~~(Oppenheimer et al., 2011; Shinohara et al., 2008)~~, and also a liquid part consisting in sulphate aerosol is present.~~.~~

Depending on the eruptive intensity, the volcanic cloud can reach different altitudes in the atmosphere thus affecting environment (Craig et al., 2016; Delmelle et al., 2002)~~ (Delmelle et al.,2002; Craig et al., 2016) ~~, climate (Bourassa et al., 2012; Haywood & Boucher, 2000; Solomon et al., 2011)~~ (Haywood et al., 2000; Solomon et al., 2011; Bourassa et al., 2012)~~, human health (Delmelle et al., 2002; Horwell et al., 2013; Horwell & Baxter, 2006; Mather et al., 2003)~~ (Delmelle et al.,2002; Mather et al., 2003; Horwell et al., 2006; 2013)~~ and aircraft safety (Casadevall, 1994). ~~(Casadevall et al., 1994; Zenher 2010).~~

The detection procedure consists in identifying the presence of certain species in the atmosphere and discriminating them against other species. Thus, volcanic ash detection is related to the discrimination of the areas (pixels in an image), which are affected by the presence of these particles. First evidences about the possibility to detect~~ the~~ volcanic cloud by means of remote sensing data arise in the eighties (A. J. Prata, 1989a; A. J. Prata~~RATA~~, 1989b)~~ (Prata, 1989a,b)~~. The method used for the detection~~ problem~~ of volcanic ash particles relies on~~in~~ the ability to discriminate between volcanic clouds and meteorological ice and ~~water vapour~~liquid water clouds by exploiting the different spectral absorption in the Thermal InfraRed (TIR) spectral range (7–14 µm).~~.~~ In this interval the absorption of ash particles with radius between 0.5 µm and 15 µm at wavelength of 11 µm is larger than the absorption of ash particles at 12 µm. The opposite happens for meteorological~~weather~~ clouds, which absorb more significantly at longer TIR wavelengths. Therefore, the Brightness Temperature Difference (BTD), i.e. the difference between the Brightness Temperatures (BTs) at 11 and 12 microns, turns out to be negative ($\Delta T_{11\mu m}$- $\Delta T_{12\mu m}$ ~~$\Delta T11\mu m$-$12\mu m$~~ < 0 °C) for regions affected by volcanic clouds and positive ($\Delta T_{11\mu m}$- $\Delta T_{12\mu m}$ > 0 °C) for regions affected by meteorological clouds.

The BTD approach is the most used method for the volcanic cloud identification. It is effective and simple to apply~~be applied~~, even if it can lead to false alarms in some cases, e.g.~~:~~ over clear surfaces during night, on soils containing large amounts of quartz (such as deserts), on very cold or ice surfaces, in the presence of high water vapour content (F. Prata et al., 2001)~~ (Prata et al., 2001a)~~. As already mentioned, the discrimination between volcanic and meteorological~~weather~~ clouds is a challenging task, since the region of the overlap of the two objects shows a mixed behaviour not easily recognizable. In these mixed scenarios, the BTD can be negative not only for volcanic clouds but also for meteorological clouds; thus, some false positive results may occur, as the case of high meteorological~~weather~~ clouds. False negative results may arise in the case of high

ha formattato: Italiano (Italia)

Codice campo modificato

Codice campo modificato

ha formattato: Danese

Codice campo modificato

Codice campo modificato

ha formattato: Pedice

ha formattato: Pedice

atmospheric water vapour content: the water vapour contribution can hide and cancel out the ash particles effects on the BTD, and then the ashy pixels cannot be revealed. In these cases a correction procedure can be applied (Corradini et al., 2008, 2009; A. J. Prata & Grant, 2001) ~~(Prata et al., 2001b; Corradini et al., 2008; 2009)~~. In addition to ~~Among~~ the described procedures ~~described~~, other algorithms ~~, based on the use of different spectral~~ algorithms~~channels,~~ have been developed (Francis et al., 2012; M. J. Pavolonis, 2010; M. Pavolonis & Sieglaff, 2012; Clarisse & Prata, 2016~~n.d.~~). ~~(Francis et al., 2012; Pavolonis et al., 2010a,b).~~

For these reasons, it seems appropriate to use advanced classification schemes to address the task of ~~the~~ ash detection, such as approaches which make use of machine learning techniques, avoiding the need to find for each product the best BTD threshold for creating the volcanic cloud mask manually, which can be a ~~considerable~~ time-consuming process.

For aerosol and meteorological cloud detection, a neural network (NN) (Atkinson & Tatnall, 1997; Bishop, 1994; Di Noia & Hasekamp, 2018) ~~(Bishop et al., 1994; Atkinson et al., 1997; Di Noia and Hasekamp, 2018)~~ based algorithm allows the solution of a classification problem. Starting from inputs containing spectral radiance values acquired in a specific wavelength band~~in specific wavelength~~, the model generates a prediction in output by assigning to each pixel of the original image a predefined class. In previous research, neural networks have already shown significant effectiveness in terms of atmospheric parameter extraction (Gardner & Dorling, 1998) and specifically for volcanic eruption scenarios ~~(Di Noia et al., 2013; Gardner & Dorling, 1998;~~ (Gray & Bennartz, 2015; Picchiani et al., 2011, 2014; Piscini et al., 2014~~; Sellitto et al., 2012~~)~~(Gardner et al., 1998; Picchiani et al., 2011; Sellitto et al., 2012; Di Noia et al., 2013; Picchiani et al., 2014; Piscini et al., 2014)~~. A strong advantage of using a NN based approach for volcanic cloud detection is that once the model is trained on a statistically representative selection of test cases, new imagery acquired over new eruptions can be accurately (depending on the training phase) classified in near real time allowing significant advantages in critical situations and in emergency management.

In this work, we developed a NN based algorithm for volcanic cloud detection using Sentinel-3 SLSTR (Sea and Land Surface Temperature Radiometer) daytime data with a model trained on MODIS (MODerate resolution Imaging Spectroradiometer) daytime images. This is possible since the two sensors have similar spectral bands and it represents an advantage as there is~~are~~ currently limited use~~amounts~~ of SLSTR products ~~available~~ for eruptive events. The use of MODIS as a proxy for SLSTR was already successfully tested in a previous work investigating the complex challenge of distinguishing ice and meteorological~~weather~~ clouds (also containing ice) using neural networks on SLSTR data (Picchiani et al., 2018) ~~(Picchiani et al., 2018)~~. As a test case, the Raikoke 2019 eruption has been considered in this work.

2 Case study: the Raikoke 2019 eruption

The Raikoke volcano is located in the Kuril Island chain, near the Kamchatka Peninsula in Russia (48.3° N, 153.2° E). On June 21, 2019 at about 18:00 UTC Raikoke started erupting and continued erupting until about 03:00 UTC on 22 June 2019). During this period, Raikoke released large amount of ash and SO_2 into the stratosphere.

ha formattato: Francese (Francia)
Codice campo modificato
ha formattato: Francese (Francia)
ha formattato: Francese (Francia)
ha formattato: Francese (Francia)
Codice campo modificato
Codice campo modificato
ha formattato: Inglese (Regno Unito)

Figure 1 shows a time-series of 11 µm brightness temperatures (BTs) determined from the Himawari-8 AHI (Advanced Himawari Imager) sensor at 10-minute intervals for the first 18 hrs of the eruption. With the purpose of searching for high (cold) vertically ascending clouds ~~associated with a vertically ascending clouds~~ due to an eruption, and not of meteorological origin, discrete eruptions were identified by comparing AHI BTs near the vent with those some distance upwind from the vent. The Himawari-8 time-series shows a sequence of eruptions (12 in all) and a sustained period of activity between 22:40 of 21 June and 02:10 of 22 June, when the majority of ash and gas was emitted. The estimated time of an eruption event was determined by examining animated images and consequently the times of eruptions shown do not always coincide with the coldest cloud-top.

It is estimated from the AHI data that June 2019 Raikoke eruption produced approximately 0.4–1.8 Tg of ash (Bruckert et al., 2022; Muser et al., 2020; A. T. Prata et al., 2022) and 1–2 Tg of SO_2 (Bruckert et al., 2022; Gorkavyi et al., 2021). ~~It is estimated from the AHI data that June 2019 Raikoke eruption produced approximately 0.4–1.8 Tg of ash and 1–2 Tg of SO_2 (Prata, private communication).~~ The amount of water vapour emitted is unknown, but would have been considerable, as ~~is~~ common in most volcanic eruptions (Glaze et al., 1997; McKee et al., 2021; Millán et al., 2022; Murcray et al., 1981; Xu et al., 2022) ~~(Murcray et al., 1981; Glaze et al., 1997; McKee et al., 2021; Xu et al., 2022; Milan et al., 2022)~~. These emissions would have led to copious amounts of water and ice clouds being produced (McKee et al., 2021; Rose et al., 1995), making the composition of the transported clouds both complex and changing with time.

~~(Rose et al., 1995; McKeee et al., 2021), making the composition of the transported clouds both complex and changing with time.~~

ha formattato: Inglese (Stati Uniti)

Codice campo modificato

ha formattato: Inglese (Stati Uniti)

ha formattato: Pedice

ha formattato: Colore carattere: Nero

ha formattato: Francese (Francia)

Codice campo modificato

Codice campo modificato

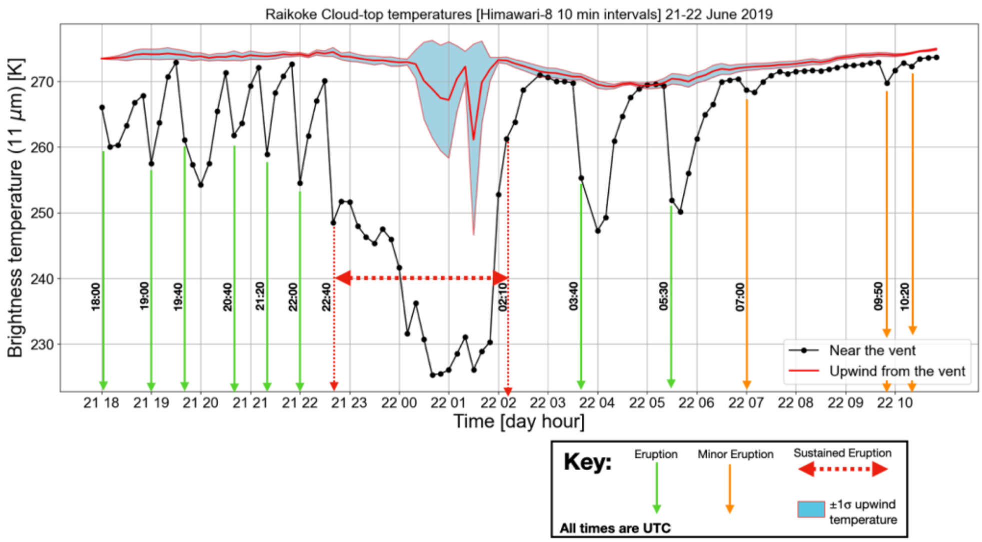

Figure 1: Time-series of eruptions from Raikoke during the first 18 hrs of activity. The times of eruptions were~~as~~ estimated from the imagery and do~~es~~ not always coincide with the coldest cloud tops. (Black line is the average within a box bounded by the latitude/longitude coordinates: 153.25-153.35°E, 48.32-48.42°N. The red line (upwind) is the average within a box bounded by: 153.10-153.20°E, 48.32-48.42°~~tops~~.

3 Instruments

In this section the specifications of the instruments which provide the products~~have been~~ used to conduct the research are described. The MODIS sensor on board Terra and Aqua satellites has been used to set up the training dataset of a NN based model. The SLSTR sensor on board Sentinel-3A and Sentinel-3B satellites has been used for the application of the aforementioned model.

3.1 MODIS i~~I~~nstrument

MODIS aboard NASA Terra and Aqua polar orbit satellites is a multispectral instrument, with 36 channels from VIS to TIR ranging from 0.4 to 14.4 µm, and spatial resolutions of 0.25 km for bands 1-2, 0.5 km for bands 3-7 and 1 km for bands 8-36. The two spacecrafts fly at 705 km of altitude in a sun-synchronous orbit, with a revisit cycle of about one or two days. Terra spacecraft was launched in 1999 and its equatorial crossing time is 10:30 am (descending node), while Aqua was launched in 2002 and its equatorial crossing time is 1:30 pm (ascending node).

ha formattato: Tipo di carattere: Grassetto, Colore carattere: Automatico

Formattato: Normale

Formattato: Normale

ha formattato: Colore carattere: Automatico

ha formattato: Colore carattere: Automatico

In our work we used several Terra-Aqua/MODIS products: Level-1A Geolocation Fields (MOD/MYD03) (see (Nishihama et al., 1997)~~, (*L1B Documents | MCST*, n.d.)[http://modis.gsfc.nasa.gov/data/atbd/atbd_mod28_v3.pdf]~~ for details), Level-1B Calibrated Radiances (MOD/MYD021KM) (see ~~[https://mcst.gsfc.nasa.gov/sites/default/files/file_attachments/M1054E_PUG_2017_0901_V6.2.2_Terra_V6.2.1_Aqua.pdf]~~ (Toller et al.~~Isaacman~~, 2017) for details), which has been used to generate the Brightness Temperatures (BTs), Level-2 Surface Reflectance (MOD/MYD09) (see (Vermote & Vermeulen, 1999) ~~[http://modis.gsfc.nasa.gov/data/atbd/atbd_mod08.pdf]~~ for details), Level-2 Cloud Product (MOD/MYD06_L2) (see ~~[https://atmosphere-imager.gsfc.nasa.gov/sites/default/files/ModAtmo/MOD06-ATBD_2015_05_01_1.pdf]~~(Menzel et al., 2015~~n.d.~~) for details).

~~MODIS aboard the NASA-Terra/Aqua polar orbit satellites is a multispectral instrument, with 36 channels from VIS to TIR, a spatial resolution from 0.25 to 1 km, and a revisit time of 1–2 days.~~

3.2 SLSTR i~~I~~nstrument

~~SLSTR is a dual view scanning radiometer, with 9 channels on board of Sentinel-3A and Sentinel-3B. The pixel size ranges from 500x500 m for VNIR and SWIR bands to 1x1 km for TIR bands.~~

The Sea and Land Surface Temperature Radiometer (SLSTR) is one of the instruments on board the Sentinel-3A (S3A) and Sentinel-3B (S3B) polar satellites launched in 2016 and 2018, respectively.

Sentinel-3 is designed for a sun-synchronous orbit at 814.5 km of altitude with a local equatorial crossing time of 10:00 am. The revisit time is 0.9 days at equator for two operational spacecrafts configuration. The orbits of the two satellites are equal but S3B flies +/- 140° out of phase with S3A. The basic SLSTR technique is inherited from the technique used by the series of conical scanning radiometers starting with the ATSR. The instrument includes the set of channels used by ATSR-2 and AATSR (0.555 – 0.865 µm for VIS channels, 1.61 µm for SWIR channel, 3. ~~3.~~74 – 12 µm for MWIR/TIR channels), ensuring continuity of data, together with two new channels at wavelengths of 1.375 and 2.25 µm in support of cloud clearing for surface temperature retrieval. The SLSTR radiometer measures a nadir and an along track scan, each of which also intersects the calibration black bodies and the visible calibration unit once per cycle (two successive scans). Each scan measures two along track pixels of 1 km (four or eight pixels at 0.5~~500~~ km resolution for visible/NIR channels and SWIR channels, respectively) simultaneously. This configuration increases the swath width in both views, as well as providing 0.5~~500~~ km resolution in the solar channels.

Our procedure makes use of the SLSTR Level-1 TOA (Top Of Atmosphere) Radiances and Brightness Temperature product from both platform S3A and S3B, see (~~Sentinel-3 SLSTR Level-1 Observables ATBD - Sentinel Online, n.d.)~~Cox et al., 2021) ~~[https://sentinels.copernicus.eu/documents/247904/2731673/S3_TN_RAL_SL_032+-Issue+8.0+version1.0-++SLSTR+L1+ATBD.pdf/fb45d35c-0d87-dca6-ea3c-dc7c2215b5bc?t=1656685672747]~~ for details of SLSTR Level-1 product.

ha formattato: Inglese (Stati Uniti)

ha formattato: Tipo di carattere: Non Corsivo

~~3~~ 4 Methodology

In this section the adopted methodology is described. The procedure has been developed in MatLab environment and the source codes are available upon request, as explained in Code Availability section. In particular, the MatLab Deep Learning Toolbox has been used to implement the NN.

A multilayer perceptron neural network (MLP NN) was trained with MODIS daytime data and then it was applied to Sentinel-3/SLSTR daytime products, in order to discriminate ashy pixels from others, following the scheme reported in Figure 2.

The MLP NN model~~structure~~ (Atkinson & Tatnall, 1997; Gardner & Dorling, 1998) ~~(Gardner et al., 1998, Atkinson et al., 1997)~~ consists in a multi-layer architecture with three types of layers. The first type of layer is the input layer, where the nodes represents the elements of a feature vector. The second type of layer is the hidden layer, and consists of only processing units~~which could be one or more layers composed of nodes~~. The third type of layer is the output layer and it represents the output data, which are the classes to be distinguished and are set to one (that of the chosen class) or zero (all other nodes) in image classification problems. All nodes (i.e. neurons) are interconnected and a weight is associated to each connection. Each node in each layer passes the signal to the nodes in the next layer in a feed-forward way, and in this passage the signal is modified by the weight. The receiving node sums the signals from all the nodes in the previous layer and elaborates them~~it~~ through an activation function before ~~to~~ passing them to the next layer.

The output of the proposed model is the SLSTR image fully classified in eight different s~~urfaces~~pecies: ash over sea, ash over cloud, ash over land, sea, land and ice surfaces, ~~water vapour~~liquid water clouds and ice clouds. This approach has been used because of the ~~long~~ readily available time series of MODIS data, the quality of MODIS products (Picchiani et al., 2011, 2014; Piscini et al., 2014) ~~(Picchiani et al., 2011; 2014; Piscini et al., 2014)~~ and the spatial/spectral similarities between MODIS and SLSTR ~~(see Table 1)~~. The SLSTR and MODIS channels which are used in our research are shown in Table 1~~Table 1~~, along with the spectral characteristics of the two sensors.

~~MODIS aboard the NASA-Terra/Aqua polar orbit satellites is a multispectral instrument, with 36 channels from VIS to TIR, a spatial resolution from 0.25 to 1 km, and a revisit time of 1–2 days. SLSTR is a dual view scanning radiometer, with 9 channels on board of Sentinel-3A and Sentinel-3B. The pixel size ranges from 500x500 m for VNIR and SWIR bands to 1x1 km for TIR bands. The feasibility of this procedure has also been confirmed for high latitudes (Picchiani et al., 2018)(Picchiani et al., 2018), since our study area is located in medium-high latitudes.~~

The first step of our procedure consists in generating the training patterns, that is the “ground truth” to be passed to the NN model during the training phase. This step represents a crucial aspect in building a NN model since the more the training dataset is accurate and representative of the problem we want to address the more the NN would be efficient in solving that problem. For this scope, MODIS products have been used as inputs to a semi-automatic procedure for identifying the different classes ~~species (i.e. classification classes)~~ to be discriminated by the NN model in the output image ~~we want the NN model be able to distinguish~~. Some of these classes~~species~~ don't exist as MODIS standard products, for example the ash classes and the

ha formattato: Norvegese (Bokmål)

ha formattato: Inglese (Stati Uniti)

Codice campo modificato

ha formattato: Inglese (Stati Uniti)

Codice campo modificato

ha formattato: Inglese (Stati Uniti)

Codice campo modificato

ice surface class;~~,~~ for this reason we derived them by means of different operations in our semi-automatic procedure developed in MatLab. Other classes~~species~~ are instead already present as MODIS standard product, for example the land/sea mask.

Table 1: Correspondence between MODIS and SLSTR channels.

SLSTR Channel	λ Centre (µm)	Bandwidth (nm)	MODIS Channel	λ Centre (µm)	Bandwidth (µm)
S1	0.554~~5~~	19.26	4	0.555	0.545-0.565
S2	0.659	19.25	1	0.659	0.620-0.670
S3	0.868~~5~~	20.60	2	0.865	0.8~~62~~41-0.87~~7~~6
S4	1.375	20.80	26	1.375	1.360-1.390
S5	1.61	60.68	6	1.64	1.628-1.652
S6	2.25	50.15	7	2.13	2.105-2.155
S7	3.74	398.00	20	3.75	3.660-3.840
S8	10.85	776.00	31	11.03	10.780-11.280
S9	12.02	905.00	32	12.02	11.770-12.270

Tabella formattata

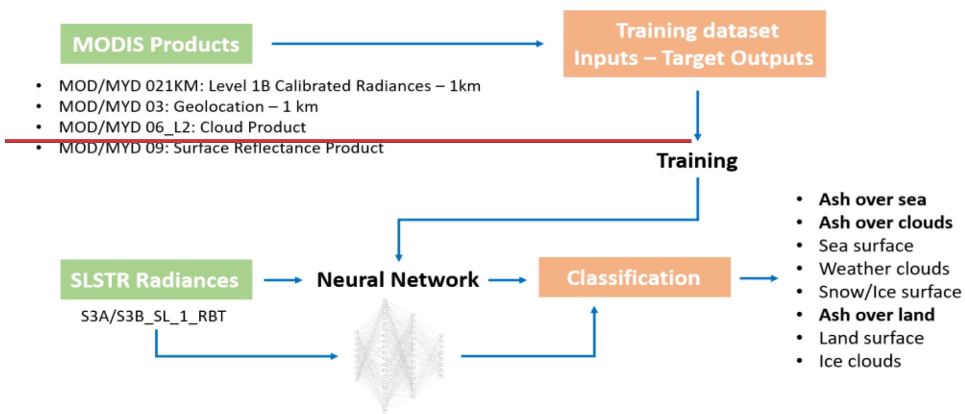

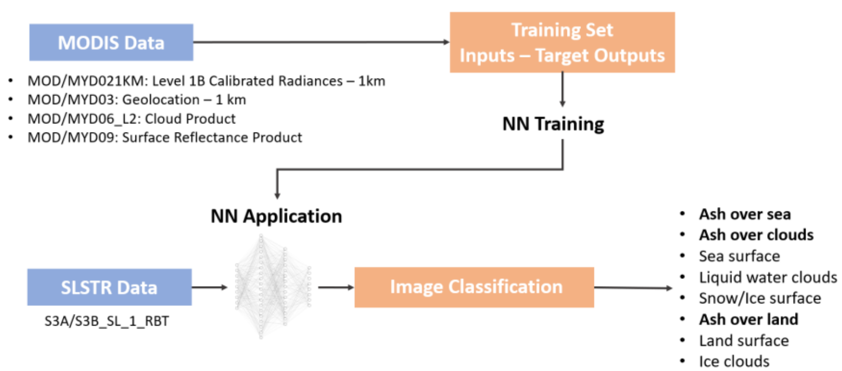

Figure 2: Overall diagram of the ~~followed~~ procedure followed for the classification process with NN model.

The training set from which we extracted the training patterns (i.e. identifying classification classes) consists of nine MODIS granules~~data~~ acquired over the Eyjafjallajokull volcano area during the 2010 eruption (from May 6^{th} to May 13^{th}), for a total of about 5400 patterns for each class available for the training of the model. The single training pattern (i.e.: training example)~~)~~ corresponds to a single pixel of a specific target class as identified in MODIS images through the semi-automatic procedure aforementioned, this means that one class is represented by several patterns. In particular, not all the pixels of the considered MODIS images are contained in the training dataset (i.e.: the ensemble of the training patterns), but only a part of them are randomly included. The total number of patterns we collected has been divided into three subsets: 75% training set, 20% validation set, 5% test set. A NN~~neural network~~ with two hidden layers of was trained and then it was applied to Sentinel-3

SLSTR RBT (Radiance and Brightness Temperature) Level 1~~(SL_1_RBT)~~ images collected during the Raikoke 2019 eruption. Table 2 shows the details of MODIS and SLSTR data used for this work.

Table 2: Training set (MODIS) from the Eyjafjallajökull 2010 eruption; Sentinel-3 Raikoke 2019 classified products.

Date	**Time UTC**	**Platform**	**Training/Application**
6 May 2010 (JD 126)	11:55	Terra	Training
9 May 2010 (JD 129)	12:25	Terra	Training
11 May 2010 (JD 131)	12:10	Terra	Training
11 May 2010 (JD 131)	12:15	Terra	Training
11 May 2010 (JD 131)	13:50	Terra	Training
11 May 2010 (JD 131)	14:05	Aqua	Training
12 May 2010 (JD 132)	12:55	Terra	Training
13 May 2010 (JD 133)	12:00	Terra	Training
13 May 2010 (JD 133)	13:40	Terra	Training
22 June 2019 (JD 173)	00:07	Sentinel-3A	Application
22 June 2019 (JD 173)	23:01	Sentinel-3B	Application

In order to build the NN training patterns a~~, the aforementioned~~~~a~~ semi-automatic procedure, that exploits MODIS radiances and standard products, has been developed. The MODIS products considered for the extraction of the training patterns are the following:

- MOD/MYD-021KM, Level 1B Calibrated Radiances – 1 km, which gives the radiance values for each MODIS band;
- MOD/MYD-03, Geolocation – 1 km, used for creating the Land/Sea Mask;
- MOD/MYD-06_L2, Cloud Product, containing cloud parameters, used for creating the Cloud Mask*;*
- MOD/MYD-09, Surface Reflectance Product, containing an estimate of the surface spectral reflectance measured at ground level; it is used for generating the Ice Mask;

where "MOD" and "MYD" stands for MODIS-Terra and MODIS-Aqua products respectively.

The semi-automatic procedure for the extraction of training patterns starting from MODIS data~~,~~ basically consists in using MODIS products to create binary "masks" identifying the different ~~objects/surfaces~~species, and then replaces them by "classes". For each element of the class~~,~~ the ~~consisting of matrices containing~~ radiance values (W/(m^2 sr µm)) are extracted from the MODIS product MOD/MYD021KM. In this way each object is radiometrically characterized. The identification of the ashy pixel is pursued by creating a mask according to specific BTD thresholds (from 0.0 to -0.4 °C) ~~and a manual correction performed through visual inspection~~ for~~of~~ each MODIS image. For this purpose, the MOD/MYD021KM product has been used to derive the brightness temperatures required to compute the BTD. The MODIS products used for training the model were acquired in near-nadir view only.

The other specie~~object~~s are identified using both MODIS Level 1 radiances~~bands~~ and MODIS standard products. Once each object/surface has been defined, they are associated with the corresponding class. Then a set of input-output samples for the training phase is generated, where the input consists of the set of radiances measured for the given pixel and the output is a binary vector with value 1 associated with the corresponding class and value 0 for the other classes.

Table 3 shows the classification map legend for each classified product presented in this work, in which eight classes are discriminated, each one representing a surface/object.

Table 3: Classification map legend.

Class ID	Surface/Object	Name	Colour
1	Ash over sea	*Ash_sea*	
2	Ash over clouds	*Ash_cloud*	
3	Sea surface	*Sea*	
4	Liquid water~~Weather~~ clouds	*Cloud*	
5	Snow/Ice surface	*Ice*	
6	Ash over land	*Ash_land*	
7	Land surface	*Land*	
8	Ice clouds	*Cloud_ice*	
-	Masked out pixels	*Not classified*	

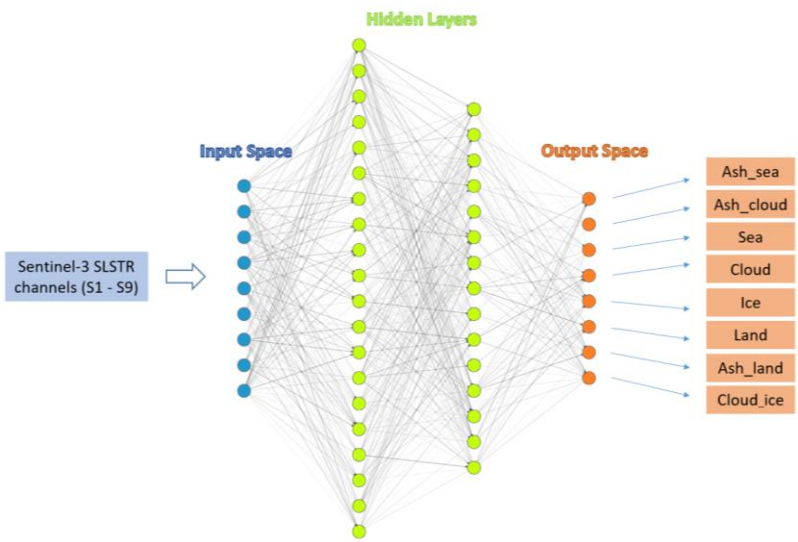

Figure 3: NN topology for ash detection.

The NN final model consists of nine inputs, which are the radiances in the SLSTR selected channels, while the output space is composed of eight classes, which are the objects/surfaces which the net has to classify. After doing several tests the optimum topology of the NN turns out to be the combination of two hidden layers with 20 and 15 neurons, respectively. For each neuron we set the hyperbolic tangent activation function (Vogl et al., 1988). The final neural network architecture used for ash detection in this work is shown in Figure 3. The proposed algorithm includes a post processing operation in order to avoid false positive results for land and sea classes. This *a~~-~~posteriori* filter is applied both to the resulting NN land and sea classes. It allows masking out the pixels which the NN classifies as land/sea which do not belong to the Sentinel-3/SLSTR land/sea mask standard product, which is always available and thus it can be used to increase the precision of the algorithm. The filtered out pixels have been inserted in a class named "not classified", as reported in Table 3 ~~Table 3~~.

For classification problems approached with machine learning algorithms, one of the most used accuracy metrics for the performance evaluation is the confusion matrix (Fawcett, 2006), where each predicted output class is compared to the corresponding ground truth considered in the validation dataset. An overall accuracy of 90.9% was obtained at the end of the NN training phase for the proposed neural network model (see Figure 4~~Figure 4~~).

ha formattato: Tipo di carattere: Corsivo

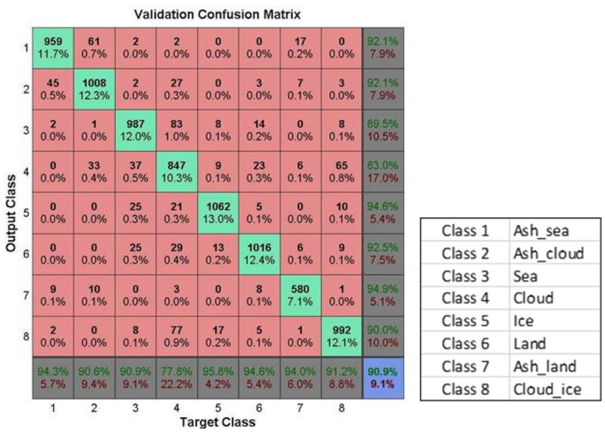

Figure 4: Confusion matrix on validation set.

The target class represents the “ground truth” of each class, while the output class refers to the prediction of the NN. The diagonal shows that most of the total of the pixels have been correctly classified (green boxes). The number of pixels incorrectly classified are placed out of the diagonal. False positives (false detection) ~~Commission~~ and ~~omission errors~~false negatives (missed detection) are reported in the last grey column and row, respectively.

The code of the procedure ran with a CPU i7-9850H (6 core, processor base frequency at 2.60 GHz):~~ and~~ it takes less than 30 minutes to~~for~~ train~~ing~~ the adopted model and~~ it takes~~ few seconds to apply it~~for applying the adopted model~~.

~~The MODIS products used for training the model were acquired in nadir view only. The trained network was applied to SLSTR products acquired both in nadir and oblique view(*Copernicus Sentinel-3 SLSTR Land User Handbook*, n.d.)(*User Guides - Sentinel-3 SLSTR - Product Grid Definitions - Sentinel Online - Sentinel Online*, n.d.).~~

~~4~~ 5 Results and Discussion

The neural network algorithm previously described was applied to Sentinel-3/SLSTR daytime images acquired on Raikoke during the 2019 eruption. The Sentinel-3A/SLSTR and Sentinel-3B/SLSTR products collected on~~the~~ 22 June 2019 at 00:07 and 23:01 UTC have been considered (see Table 2).

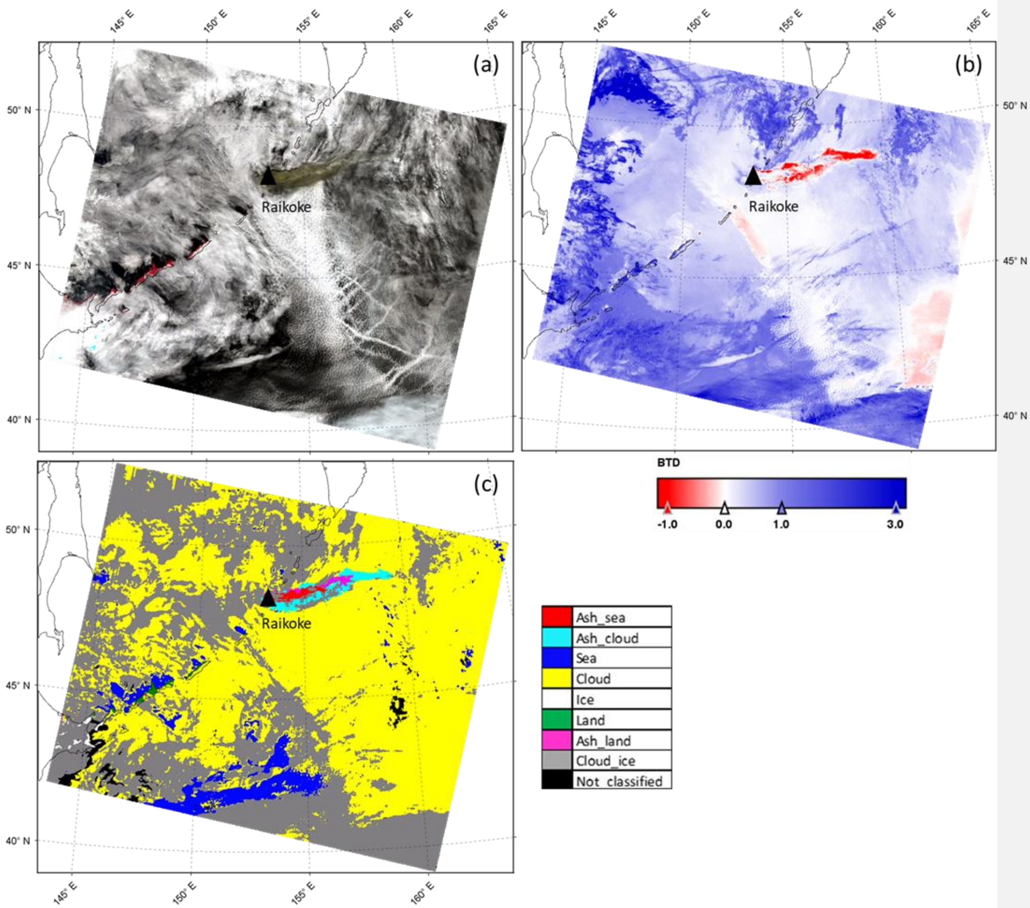

Figure 5: Sentinel-3A/SLSTR image collected on Raikoke for~~the~~ 22 Jun 2019 at 00:07 UTC, nadir view. (a) RGB; (b): BTD; (c): NN classification.

Figure 5(a) shows the RGB colour composite of the S3A/SLSTR image acquired on Raikoke for~~the~~ 22 June 2019 at 00:07 UTC. The RGB composite has been carried out by considering the SLSTR visible (VIS) channels S3 (868 nm), S2 (659 nm) and S1 (554 nm) for R, G and B, respectively. In Figure 5(b) the BTD map is displayed, where red and blue pixels represent negative and positive BTD, respectively. The BTD is computed by making the difference between the brightness temperature of the SLSTR thermal infrared channels S8 and S9 centred at 10.8 and 12 μm. The output of the NN classification is shown in Figure 5(c) with the corresponding colour legend, where each colour represents the classified surface/object.

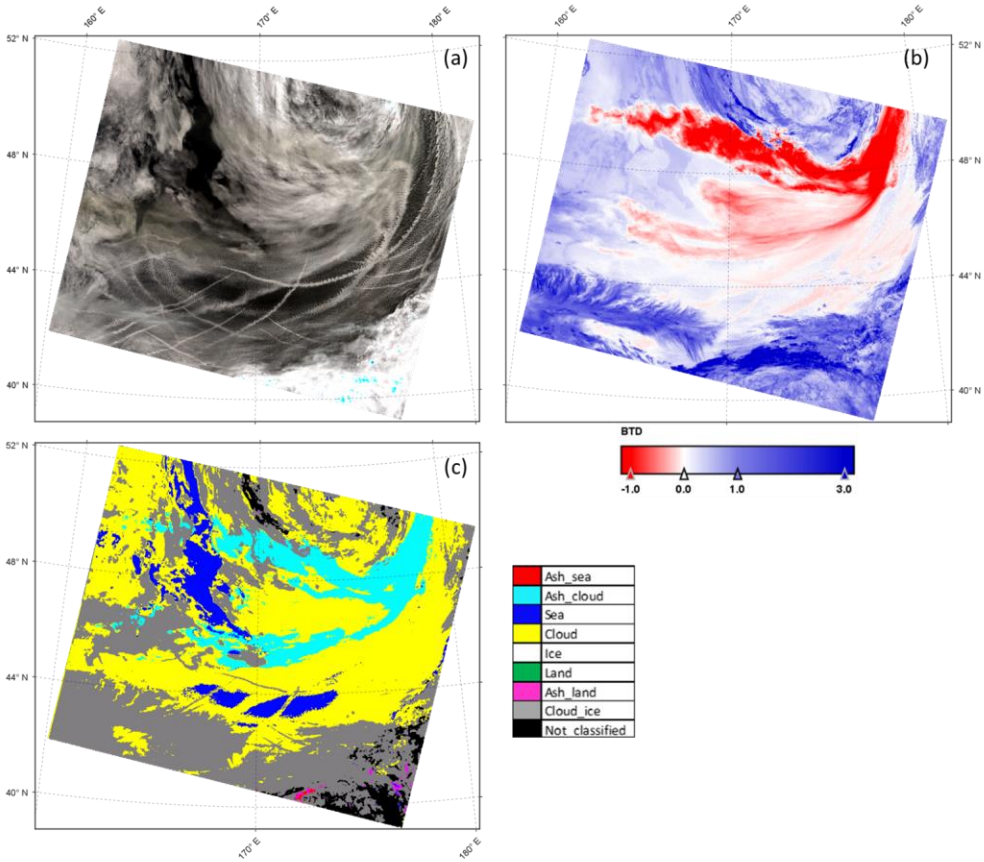

Figure 6: Sentinel-3B/SLSTR image collected on Raikoke for~~the~~ 22 June 2019 at 23:01 UTC, nadir view. (a): RGB; (b): BTD; (c): NN classification.

As Figure 5(a) shows, the RGB composite show~~emphasize~~s the presence of a wide distribution of meteorological clouds and a significant signal derived from the volcanic cloud (brown pixels). The BTD (Figure 5(b)), obtained with a threshold of 0 °C, shows the presence of the volcanic cloud together with a significant number of false negatives (volcanic cloud pixels not identified near the vents) and false positives (pixels identified as volcanic cloud while actually they~~but that~~ are not, see light red pixels below the volcanic cloud and along the right edge of the scene)~~ pixels~~.

Despite the challenging scenario, the NN algorithm shows its ability to detect the volcanic cloud and to classify the whole image, by detecting with good accuracy meteorological clouds composed of water droplets (yellow) and ice (grey), sea (blue) and land (green) surfaces, and volcanic ash clouds, as reported in Figure 5(c). Looking at the cloud masks generated with the NN algorithm (yellow and grey) and by comparing them with the RGB natural colour composite of the SLSTR product, a high degree of agreement in terms of spatial features can been observed. From the comparison between NN output classes and RGB composite we can observe that also land (green) and sea (blue) pixels are properly detected in the areas where they actually lie.

From a qualitative comparison between the NN plume mask and the RGB composite, we can state that the NN correctly identifies the volcanic cloud class in the area where it seems actually present, even if some pixels are misclassified as ash ~~-~~over~~n-l~~ land (magenta pixels), instead of ash above meteorological cloud. As Figure 5 shows, the NN algorithm is able to detect a wide volcanic cloud area and ~~much less false positives~~more ash, especially in the opaque regions, compared to the BTD approach. In particular the difference found near the vents can be due to the complete opacity of the cloud. Here the ash cloud optical thickness is so high that there is no spectral difference and the BTD approach has no sensitivity~~ is null~~.

Following the same visualization scheme of Figure 5, the results derived from the application of the trained NN model to the S3B/SLSTR image acquired on~~the~~ 22 June 2019 at 23:01 UTC are reported in Figure 6. In this second image, all the ashy pixels are classified by the NN model as ash above meteorological clouds (cyan pixels). This seems reasonable being the scenario mostly dominated by meteorological~~weather~~ clouds, as we can also observe looking at the NN classification, which assigns the majority of the pixels to the ~~water vapour~~liquid water cloud class (yellow) and to the ice cloud class (grey). The NN classification shows also the presence of sea pixels (blue), which are located in the same area identifiable using the RGB composite. In this case, from the RGB composite (Figure 6(a)), unlike ~~to~~ what is seen in the 00:07 UTC~~ can be seen in the midnight~~ image, it is not straightforward to identify the volcanic plume by visual inspection. Indeed, this image was collected about 24 hours later than the previous one and thus the plume has been transported through the atmosphere and dispersed. A qualitative comparison between the NN classification (Figure 6(c)) and the BTD map (Figure 6(b)) shows considerable differences between the two methods. The BTD, obtained with a threshold of 0 °C, identifies a wider area (red pixels) affected by the volcanic cloud with respect to the NN ash mask (cyan pixels). We can notice that the BTD map includes some ~~aerial trails~~aircraft condensation trails (recognizable by the shape in the RGB composite) in the ash mask, which ~~represent of course~~can be identified as false ~~positive results~~ash detections. The reasons for these ~~false positives~~misclassifications are not fully understood, but may be due to multilayer cloud effects, pixel heterogeneity or viewing angle.

~~Figure 7 shows the RGB composite and the NN classification for the SLSTR oblique view product collected the 22 June 2019 at 00.07 UTC (Figure 7(a) and Figure 7(b)) and 23.01 UTC (Figure 7(c) and Figure 7(d)) respectively.~~

~~Looking at results obtained for the oblique view (Figure 7), we can observe that for the S3B/SLSTR image collected the 22 June 2019 at 23.01 UTC the NN model produces good results, which are also in accordance to the NN output obtained for the~~

~~processing of nadir view image acquired at the same time. For the S3A/SLSTR image collected the 22 June 2019 at 00.07 UTC, the NN results are instead less accurate; this is due to the opacity of the volcanic cloud.~~

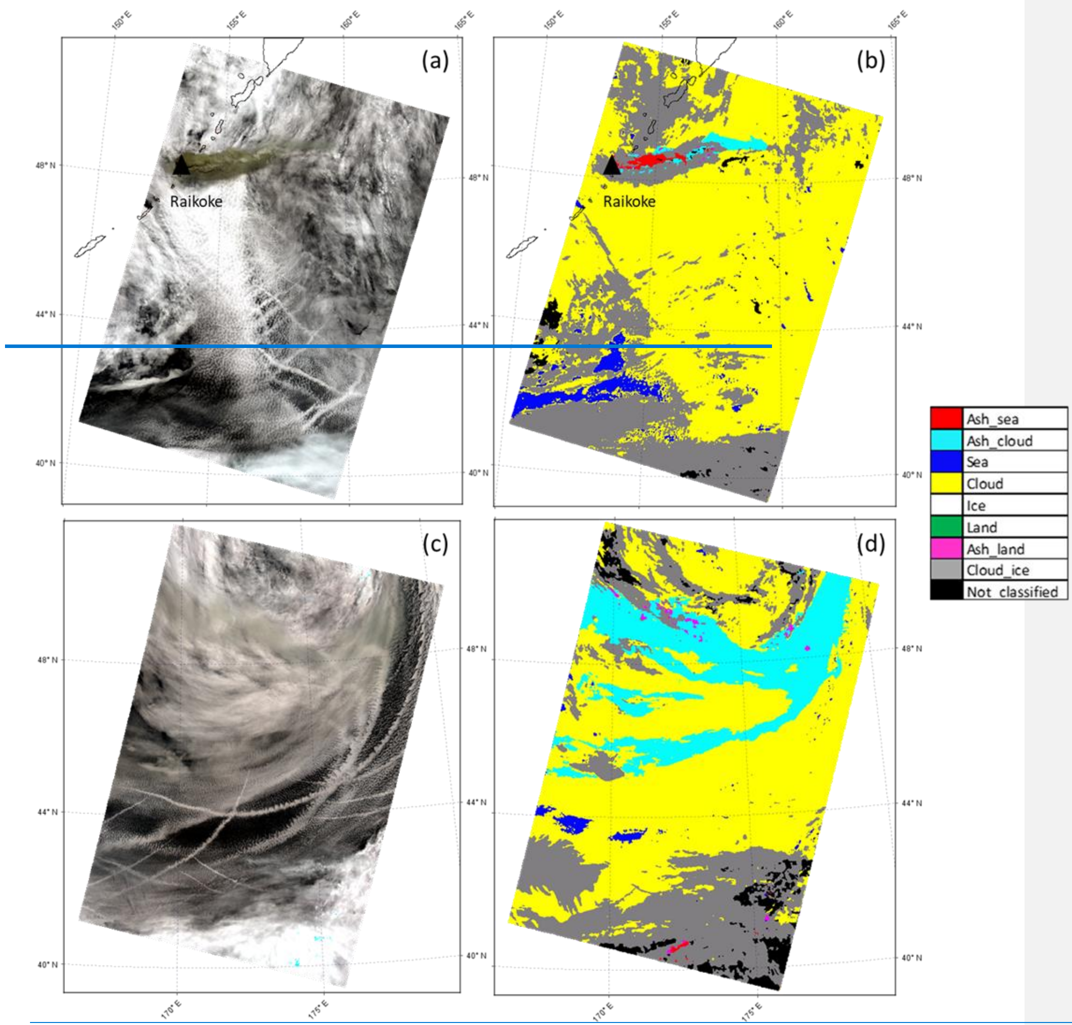

~~**Figure 7:** Sentinel-3A/SLSTR image collected on Raikoke the 22 Jun 2019 at 00:07 UTC, oblique view ((a) and (b)); Sentinel-3B/SLSTR image collected on Raikoke the 22 June 2019 at 23:01 UTC, oblique view ((c) and (d)). (a) and (c): RGB; (b) and (d): NN classification.~~

~~A significant point to be discussed is that the results obtained in this work highlighted the robustness and transferability for a NN model learning from one single event in a specific location in the world with specific background condition (latitude, longitude, geometry of acquisition, atmospheric condition, season, etc) and successfully operating in a different scenario.~~ Our results suggest that the NN technique is robust and has shown that it is possible to transfer the NN model from one single eruption event to others occurring at similar latitudes. However, the complexity of the application suggests that the generalization of the methodology to all types of eruptions is not straightforward. For example, the change of latitude has an impact on the characteristics of the atmosphere. At the same time different volcanoes emit different types of ash affecting the variability of the radiance values detected by the sensors. A possible solution to give to the proposed technique a broader applicability could be ~~the~~ training ~~of~~ different NN models for specific latitude belts which can be defined to cover the whole globe.

Overall, we can summarize the main uncertainties and the limitations of the presented model in the following points:

1. model transferability is significantly related to the spatial-temporal data availability for the generation of a training dataset which is statistically representative of all the possible scenarios;
2. lack of standard ground truth data for training and validation phases requires the BTD threshold selection by an operator which prevents the method from being fully objective.

ha formattato: Car. predefinito paragrafo, Colore carattere: Automatico

ha formattato: Car. predefinito paragrafo, Colore carattere: Automatico, Motivo: Trasparente

ha formattato: Car. predefinito paragrafo, Colore carattere: Automatico

ha formattato: Car. predefinito paragrafo, Colore carattere: Automatico

ha formattato: Colore carattere: Automatico

ha formattato: Car. predefinito paragrafo, Colore carattere: Automatico

Formattato: Paragrafo elenco, Numerazione automatica + Livello:1 + Stile numerazione: 1, 2, 3, … + Comincia da:1 + Allineamento: A sinistra + Allinea a: 0.25" + Imposta un rientro di: 0.5"

~~4~~5.1 Vicarious v~~V~~alidation

The capability of the NN to correctly detect pixels containing ash was validated by making a pixel per pixel comparison with a reference plume mask generated manually (hereafter MPM) in order to obtain the best accurate *ground truth* as possible in each SLSTR product. The choice of taking the MPM as reference derives from the lack of ash standard products.

For the image collected at 00:07 UTC the MPM creation was performed by selecting a region around the volcanic cloud (clearly recognizable as it is at the beginning of the eruption) and then considering only the pixels with 11 μm brightness temperature < 270 K (see Figure 1). In this case the BTD alone it is not very useful as the high value of the ash optical thickness of the cloud (especially close to the vent) produces many pixels with BTD values near zero, not distinguishable from adjacent pixels characterized by meteorological clouds. For the image collected at 23:01 UTC, the identification of the volcanic cloud is much more difficult due to its larger spread and dilution; in this case the MPM was obtained considering the pixels with BTD < -0.25 °C, even if probably this choice implies that some ashy pixels were discarded. On the other hand, using an higher BTD threshold will produce a lot of false positive pixels. In general, the creation of an accurate manual plume mask is time consuming and case-sensitive and often requires the presence of an operator; so the generation of a volcanic cloud mask with a fast, automatic and case-independent procedure would be a rather significant improvement.

Because the MPM doesn't distinguish between the different surfaces under the ash cloud, the validation is performed by considering the total of the ashy pixels detected from the NN (i.e. the sum between *ash_land*, *ash_sea* and *ash_cloud*).

Figure 7~~Figure 8~~ shows the MPM, created as described above, and the comparison between NN plume mask (hereafter NNPM) and MPM for the S3A/SLSTR image collected on Raikoke for~~the~~ 22 June 2019 at 00:07 UTC (Figure 7~~Figure 8~~(a) and Figure 7~~Figure 8~~(b)) and S3B/SLSTR image collected on Raikoke for~~the~~ 22 June 2019 at 23:01 UTC (Figure 7~~Figure 8~~(c) and Figure 7~~Figure 8~~(d)).

~~In relation to the images which display the comparison between NN output and MPM (Figure 8(b) and Figure 8(d)), green areas indicate the pixels for which both the MPM and NN ash masks detect the presence of volcanic cloud, red pixels represent the areas classified as ash only by the MPM; blue ones are the pixels classified as ash only according to the NN model. We can observe that most of the volcanic cloud is displayed in green for both products (00.07 UTC and 23.01 UTC), indicating good matching between the two approaches. This is also confirmed by the scores in Table 4, which shows the number of pixels classified as ash by both NN and MPM (green pixels), the number of pixels classified as ash only by NN (blue pixels), the number of pixels classified as ash only by MPM (red pixels). We can observe that the two approaches are in accordance for the majority of the pixels, albeit they differ in discriminating volcanic cloud in some regions.~~

Table 4: NN and BTD volcanic cloud detection accuracies using classification metrics derived from the c~~C~~omparison between the ~~NN~~ plume mask obtained from the two approaches and ~~(NNPM) and~~ the manual plume mask (MPM) for each SLSTR considered~~lassified~~ product ~~(pixels number for each class)~~, respectively. ~~The total number of classified pixels is 1614405 for the S3A/SLSTR at 00.07 UTC image and 1701319 for the S3B/SLSTR at 23.01 UTC image respectively.~~

~~**Product**~~ **Classified Product**	~~**Ash**~~ **~~P~~plume mask source**	**Precision**~~**NNPM and MPM**~~	~~**Only NNPM**~~**Recall**	~~**Only MPM**~~**F-measure**	**Accuracy**
S3A/SLSTR at 00:~~.~~07 UTC	NN classification	0.709~~13545~~	0.683~~5568~~	0.696~~6275~~	0.993
S3A/SLSTR at 00:07 UTC	BTD < 0 °C	0.164~~136435~~	~~39991~~0.647	~~71223~~0.261	0.955
S3B/SLSTR at 23:01 UTC	NN classification	0.773	0.657	0.710	0.935
S3B/SLSTR at 23:01 UTC	BTD < 0 °C	0.417	0.998	0.588	0.829

Tabella formattata

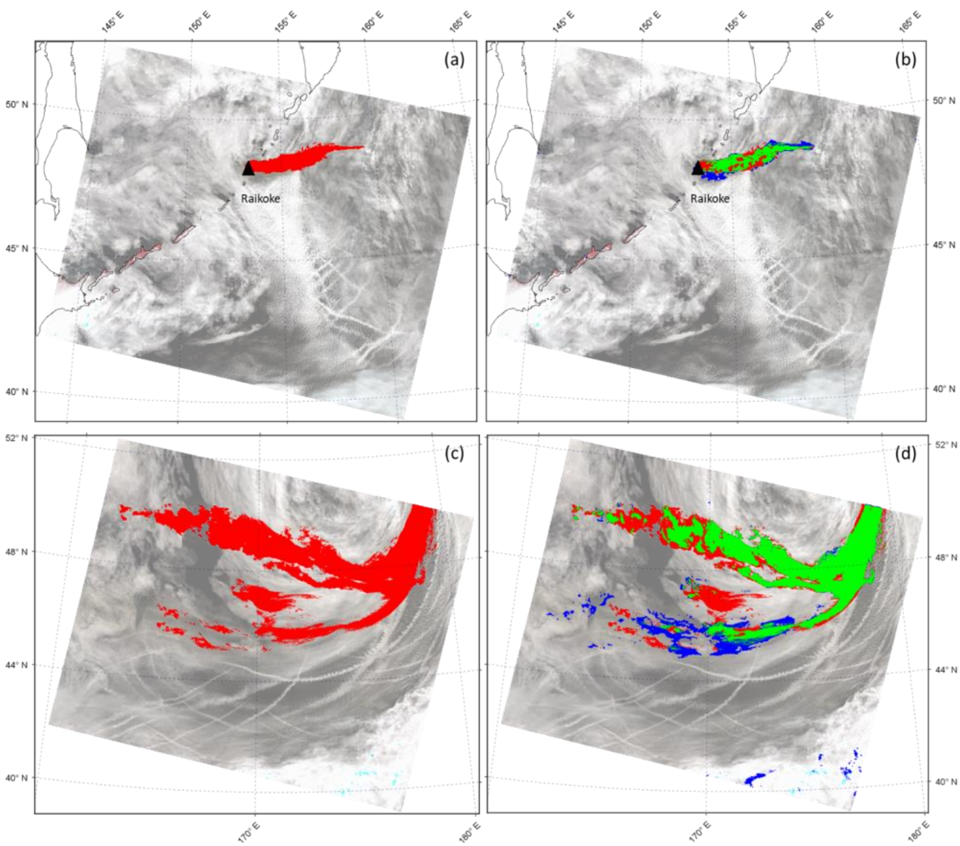

Figure 78: Sentinel-3A/SLSTR image collected on Raikoke for ~~the~~ 22 June 2019 at 00:07, nadir view (a),(b); Sentinel-3B/SLSTR image collected on Raikoke for~~the~~ 22 June 2019 at 23:01, nadir view (c),(d). (a),~~,~~(c): red pixels display the manual plume mask (MPM) obtained from the analysis on the specific image; (b),(d): comparison between volcanic ash detected by NN and MPM; green pixels indicate the areas for which both NN and MPM detect ashy pixels, red pixels indicate the areas for which only MPM detects ashy pixels, blue pixels indicate the areas for which only NN detects ashy pixels.

Formattato: Normale

~~Besides the NN plume mask validation, we also compared the pixels which the NN model classified as affected by meteorologicalweather clouds (hereafter NNCM) with the SLSTR standard product for meteorological clouds.~~

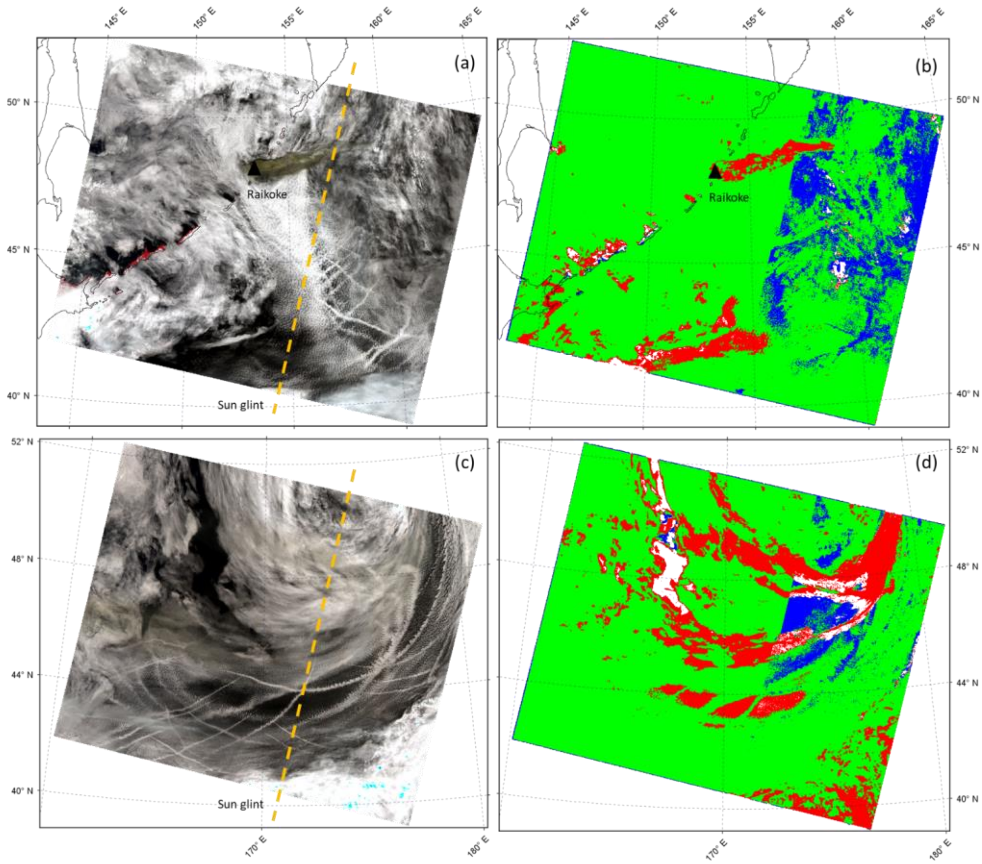

Figure 8~~9~~: Sentinel-3A/SLSTR image collected on Raikoke for~~the~~ 22 June 2019 at 00:07, nadir view (a),(b); Sentinel-3B/SLSTR image collected on Raikoke for~~the~~ 22 June 2019 at 23:01, nadir view (c),(d). (a),(c): RGB view; (b),(d): comparison between cloud mask retrieved by NN and standard Sentinel-3 confidence in summary cloud mask (CSCM); green pixels indicate the areas for which both NN and CSCM detect cloudy pixels, red pixels indicate the areas for which only CSCM detects cloudy pixels, blue pixels indicate the areas for which only NN detects cloudy pixels, white pixels indicate the areas for which both NN and CSCM don't detect ~~the presence of~~ cloudy pixels.~~.~~

In relation to the images which display the comparison between NN output and MPM (Figure 7~~Figure 8~~(b) and Figure 7~~Figure 8~~(d)), green areas indicate the pixels for which both the MPM and NN ash masks detect the presence of volcanic cloud, red pixels represent the areas classified as ash only by the MPM; blue pixels are classified as ash only according to the NN model. We can observe that most of the volcanic cloud is displayed in green for both products (00:07 UTC and 23:01 UTC), indicating good agreement between the two approaches. This is also confirmed by the scores in Table 4, which allow quantitative conclusions on the accuracy of the proposed NN model ~~–~~approach compared to the MPM considered as *ground truth*. The classification metrics considered are precision, recall, F-measure and accuracy (Fawcett, 2006) which range from 0 to 1 (perfect classifier).

The~~ performance~~ score differences for the two classified products are mainly related to the significant higher number of correctly classified ashy pixels contained in the 23:01 UTC (136435 pixels) with respect to 00:07 UTC (13545 pixels), if compared to the total number of classified pixels in the images which is similar (1614405 pixels for the S3A/SLSTR at 00:07 UTC image and 1701319 for the S3B/SLSTR at 23:01 UTC image respectively). However, the metrics are aligned for both ~~the ~~classified data with encouraging values for each index suggesting the reasonability of the results. In particular, the F-measure results of around 0.7 for both~~ the~~ classifications. Moreover, using MPM as a benchmark, the comparison of the metrics obtained with the BTD < 0°C approach with those derived with the NN model indicates that the neural network performs a more accurate volcanic cloud detection for both~~ the~~ considered test cases.

Besides the NN plume mask validation, we also compared the pixels which the NN model classified as affected by meteorological clouds (hereafter NNCM) with the SLSTR standard product for meteorological clouds.

Among the cloud masks available in the SLSTR L1RBT product, the *confidence_in_summary_cloud* mask (hereafter CSCM) is considered. The CSCM is a cloud mask which discriminates cloud pixels (*true*) and cloud-free pixels (*false*); it is an ultimate cloud mask product derived from several separated cloud tests (Polehampton et al., 2021)~~(*Copernicus Sentinel-3 SLSTR Land User Handbook*, n.d.)(Sentinel-3-SLSTR-Land-Handbook, 2021)~~. As~~Because of~~ the CSCM doesn't distinguish between meteorological liquid water~~meteo~~ clouds and meteorological~~meteo~~ ice clouds as the NN algorithm does, the comparison is realized by considering the whole NN meteorological~~meteo~~ cloud classes (i.e. the sum between *Cloud* and *Cloud_ice*).

Figure 8~~Figure 9~~ displays the RGB composite, in which the Sentinel-3 sun glint mask is highlighted (right part of the scene), and the comparison between NN cloud mask and S3 cloud mask for S3A/SLSTR image collected on Raikoke for~~the~~ 22 June 2019 at 00:07 UTC (Figure 8~~Figure 9~~(a) and Figure 8~~Figure 9~~(b)) and for S3B/SLSTR image collected on Raikoke for~~the~~ 22 June 2019 at 23:01 UTC (Figure 8~~Figure 9~~(c) and Figure 8~~Figure 9~~(d)).

Also in this case, for the images displaying the comparison between the two types of cloud masks (Figure 8~~Figure 9~~(b) and Figure 8~~Figure 9~~(d)), green indicates the pixels classified as meteorological cloud for both procedures, while red and blue indicate the pixels classified as meteorological cloud only from the SLSTR standard product and NN, respectively. Pixels that are not coloured are associated to a cloud-free condition for both the NN and the S3 cloud mask. Looking at the comparison, a very good agreement between the NN meteorological~~meteo~~ cloud mask and the SLSTR standard cloud mask can be observed.

The metrics in ~~Table 5,~~ Table 5 show very good performances, reaching an F-measure around 0.9~~with high amount of pixels~~

ha formattato: Tipo di carattere: Corsivo

~~classified as affected by clouds by both products (see~~ Table 5~~)~~. Moreover, looking at the red pixels in the 23:01 UTC image especially, it can be noted that the SLSTR cloud mask ~~includes~~ also includes the volcanic cloud.

Codice campo modificato

Table 5: NN meteorological cloud detection accuracy using classification metrics derived from the c~~C~~omparison between the NN cloud mask (NNCM) and the confidence in summary cloud mask (CSCM) for each SLSTR considered~~classified~~ product ~~(pixels number for each class)~~which has been assumed as ground truth.~~ The total number of classified pixels is 1614405 for the S3A/SLSTR at 00.07 UTC image and 1701319 for the S3B/SLSTR at 23.01 UTC image respectively.~~

~~Product~~ Classified Product	Precision~~NNCM and CSCM~~	~~Only NNCM~~Recall	~~Only CSCM~~F-measure	Accuracy
S3A/SLSTR at 00:~~.~~07 UTC	0.891~~1332632~~	0.936~~163225~~	0.913~~91768~~	0.842
S3B/SLSTR at 23:~~.~~01 UTC	0.952~~1291989~~	~~65359~~0.820	~~284193~~0.881	0.795

Tabella formattata

From the validation procedure we have carried out, a considerable point which has to be underlined is that, unlike adopting a time consuming and case-specific approach as MPM which also needs a manual operation by setting various thresholds for each case under examination, the NN model can be used to discriminate ash plume in satellite images with good accuracy in a fast and automatic way, which saves a significant amount of time~~. The extra speed is obtained~~ by eliminating the need for manual intervention.

~~5~~ 6 Conclusions

In this work the results of a new neural network based approach for volcanic cloud detection are described. The algorithm, developed to process Sentinel-3/SLSTR daytime images, exploits the use of MODIS daytime data as training. The procedure allows the full characterization of the SLSTR image by identifying, besides the ~~the~~ volcanic cloud, ~~the~~ surfaces under the cloud itself, ~~the~~ meteorological clouds (and phases), land, and sea surfaces. As test cases, the S3A-S3B/SLSTR images collected over the Raikoke volcano area during the June 2019 eruption have been considered.

The proposed neural network based approach for volcanic ash detection and image classification shows an overall good accuracy for the ash class, which is the main target of the algorithm, and for the meteorological cloud class as well~~also~~. A strong effectiveness of the NN classification is indeed also related to the cloudy pixel recognition, with the ability to distinguish two different types of meteorological clouds composed of water droplets and ice respectively. It has to be reminded that the wide distribution of meteorological clouds in the scenario under consideration makes the ash detection task particularly complex.~~, since meteorologicalweather ice clouds and volcanic clouds exhibit similar spectral behaviour.~~

A point to be underlined is the valuable advantage of the ~~developed~~ procedure related to the creation of products (the eight classes) not all currently~~already~~ available as SLSTR standard products; this fact represents a considerable step forward for generation of novel types of S3/SLSTR products.

A post processing has been applied to NN outputs by exploiting the land/sea mask available in the~~of~~ SLSTR standard products, in order to mitigate the insurgence of NN land/sea failure~~, being the land/sea mask~~ which is ~~always available as SLSTR standard product~~.

The comparison between the NN plume mask and a reference plume mask (MPM) taken as *ground truth*, shows a good agreement between the two techniques. The significant result lies in the fact that the overall good performance of the NN output is achieved in an automatic way and with a brief processing time, compared to the plume mask specifically generated ~~ad hoc~~, which instead requires a longer time, is case-specific and ~~it~~ needs the presence of an operator. The other considerable achievement of the NN developed procedure ~~indeed~~ is that, once the NN model has been properly trained, it has been used to detect the ash plume for each SLSTR image related to the Raikoke eruption, while the creation of the MPM has to be made separately for each image.

The comparison between the NN cloud mask and the cloud mask derived from SLSTR standard products has ~~been~~ also been carried out, resulting in a high percentage of agreement between the two products.

~~We also aim at further investigating some aspects in order to improve the classification accuracy, as the introduction of other output classes, such as volcanic ice cloud, and the integration of other variables in the model, such as the sensor view angle.~~

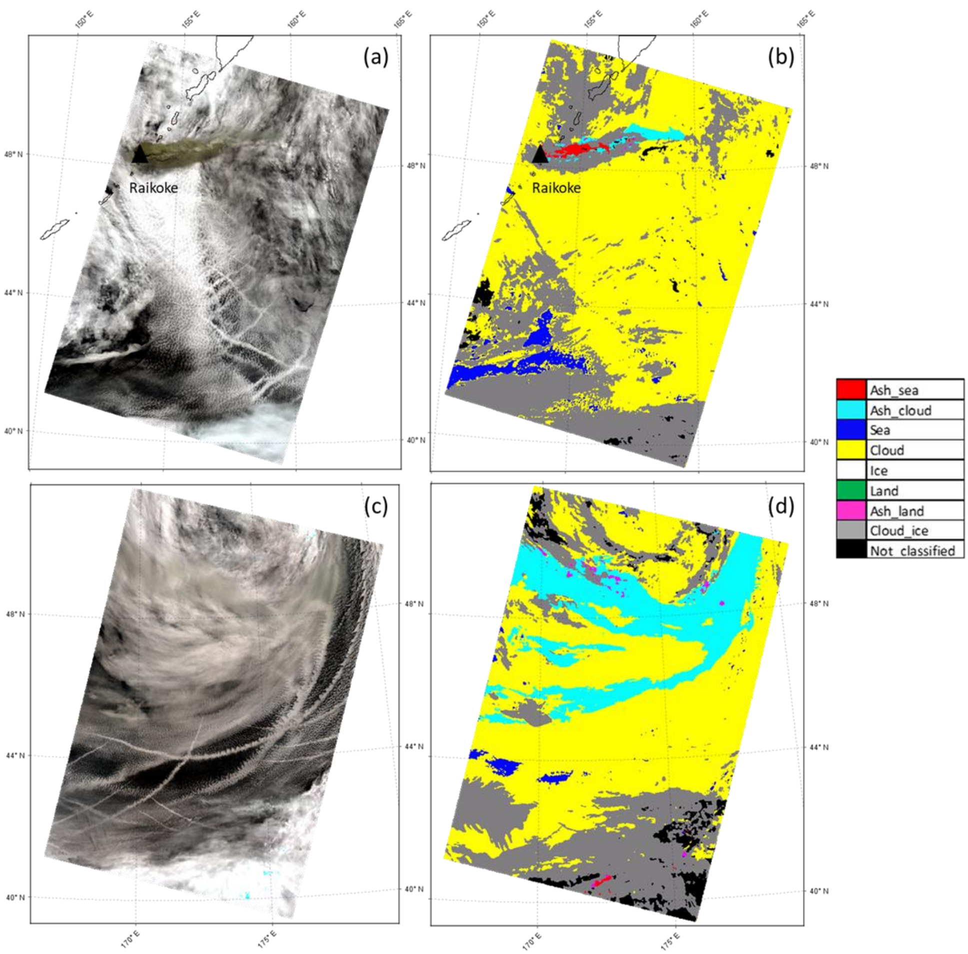

Figure 9~~7~~: Sentinel-3A/SLSTR image collected on Raikoke for 22 Jun 2019 at 00:07 UTC, oblique view ((a) and (b)); Sentinel-3B/SLSTR image collected on Raikoke for 22 June 2019 at 23:01 UTC, oblique view ((c) and (d)). (a) and (c): RGB; (b) and (d): NN classification.

A promising~~ly~~ outcome is related to the ability of the NN model to generalize over different data in terms of spatio-temporal and geographical characteristics, being the NN model trained with data collected over the Iceland region in 2010 and then applied to data acquired over the Kamchatka Peninsula in Russia in 2019. Something~~One of the point~~ under consideration for future improvements is to enhance the ability of the NN to generalize over various eruptive scenarios, by integrating different training dataset (in terms of regions, type of eruption, time interval, etc). In fact, the current methodology has been applied just to ~~just~~ a few test cases and more validation is required in order to give the technique broader applicability. For example, the effects of varying moisture and atmospheric conditions has not been fully explored. On the other hand, the generation of an appropriate number of examples, which must be statistically representative of all the possible scenarios, to be included in the training dataset may represent a very difficult task. A possible approach could be the design of different neural networks, each associated with a specific scenario.

We also aim at further investigate some aspects in order to improve the classification accuracy, as the introduction of other output classes, such as volcanic ice cloud, and the integration of other variables in the model, such as the sensor view angle. Moreover, a fully comprehensive study about the sensitivity of the NN detection on~~to~~ the observation angle could be another possible future development~~s~~ of the study. Here we addressed briefly this point applying the trained network to SLSTR oblique view products, characterized by a zenith view angle of about 55° (Polehampton et al., 2021). ~~Figure 7~~ shows the RGB composite and the NN classification for the SLSTR oblique view product collected on 22 June 2019 at 00:07 UTC (~~Figure 7~~(a) and ~~Figure 7~~(b)) and 23:01 UTC (~~Figure 7~~(c) and ~~Figure 7~~(d)) respectively. It is interesting, as a preliminary result, to show how, especially for the 23:01 UTC image where the opacity of the volcanic cloud is slighter, the main features of the classification map obtained using a NN model trained only on near nadir view acquired products and used for classifying oblique view data are mostly conserved. However, the complexity brought in by the difference in the slant optical depth, which may translate to a noticeable difference in top-of-atmosphere signal levels, needs to be investigated in a full dedicated study.

~~Finally, the possibility to use S3/SLSTR products as training dataset instead of using MODIS data is an essential point to be taken into account in order to increase the accuracy of the algorithm.~~Finally, the possibility to use S3/SLSTR products to train~~for training~~ a neural network able to detect volcanic clouds in Sentinel-3/SLSTR granules might improve the overall accuracy of the classification.

Code availability

The whole methodology is developed in MatLab environment. The source codes are available upon request to ilaria.petracca@uniroma2.it.

Data availability

Terra-Aqua/MODIS data are distributed from the Level-1 and Atmosphere Archive & Distribution System (LAADS) Distributed Active Archive Center (DAAC) and they are available at: https://ladsweb.modaps.eosdis.nasa.gov/search/.

ha formattato: Car. predefinito paragrafo, Colore carattere: Nero, Motivo: Trasparente

ha formattato: Colore carattere: Automatico

ha formattato: Car. predefinito paragrafo, Colore carattere: Automatico, Motivo: Trasparente

ha formattato: Car. predefinito paragrafo, Colore carattere: Nero, Motivo: Trasparente

ha formattato: Car. predefinito paragrafo, Colore carattere: Nero, Motivo: Trasparente

ha formattato: Colore carattere: Nero

ha formattato: Colore carattere: Nero

ha formattato: Colore carattere: Nero

ha formattato: Colore carattere: Nero

ha formattato: Colore carattere: Nero

Codice campo modificato

Codice campo modificato

Codice campo modificato

Codice campo modificato

Codice campo modificato

ha formattato: Tipo di carattere: Grassetto, Colore carattere: Nero

ha formattato: Inglese (Regno Unito)

ha formattato: Tipo di carattere: Grassetto

Sentinel-3/SLSTR data are distributed from the Copernicus Open Access Hub and they are available at: https://scihub.copernicus.eu/dhus/#/home.

The dataset used for this study are freely available on the Zenodo platform (https://doi.org/10.5281/zenodo.7050771).

Author contributions

IP and DDS developed algorithms, analyzed data and results and wrote the manuscript; MP developed algorithms and methodology, analyzed data and results and reviewed the manuscript; SC and LG analyzed data and results, provided reference data for validation task and wrote-reviewed the manuscript; FP supported the analysis of data and results, worked on the Himawari-8 analysis ~~and on the relative~~ part of the manuscript, and reviewed the manuscript; LM and DS supported the analysis of data and results; FDF reviewed the manuscript, supervised the research and contributed to funding acquisition; GSal supported the analysis of data and results and worked on validation; GSch supports the research and contributed to funding acquisition.

All authors have read and agreed to the published version of the manuscript.

Competing interests

The authors declare that they have no conflict of interest.

Disclaimer

Publisher’s note: Copernicus Publications remains neutral with regard to jurisdictional claims in published maps and institutional affiliations.

Special issue statement

This article is part of the special issue “Satellite observations, in situ measurements and model simulations of the 2019 Raikoke eruption (ACP/AMT/GMD inter-journal SI)”. It is not associated with a conference.

Acknowledgments

The results shown in this work were obtained in the framework of the VISTA (Volcanic monItoring using SenTinel sensors by an integrated Approach) project, which was funded by ESA within the “EO Science for Society framework” [https://eo4society.esa.int/projects/vista/].

Financial support

Not applicable.

References

Atkinson, P. M., & Tatnall, A. R. L. (1997). Introduction Neural networks in remote sensing. *International Journal of Remote Sensing*, *18*(4), 699–709. https://doi.org/10.1080/014311697218700

Bishop, C. M. (1994). Neural networks and their applications. *Review of Scientific Instruments*, *65*(6), 1803–1832. https://doi.org/10.1063/1.1144830

Bourassa, A. E., Robock, A., Randel, W. J., Deshler, T., Rieger, L. A., Lloyd, N. D., Llewellyn, E. J. (Ted), & Degenstein, D. A. (2012). Large Volcanic Aerosol Load in the Stratosphere Linked to Asian Monsoon Transport. *Science*, *337*(6090), 78–81. https://doi.org/10.1126/science.1219371

Bruckert, J., Hoshyaripour, G. A., Horváth, Á., Muser, L. O., Prata, F. J., Hoose, C., & Vogel, B. (2022). Online treatment of eruption dynamics improves the volcanic ash and SO_2 dispersion forecast: Case of the 2019 Raikoke eruption. *Atmospheric Chemistry and Physics*, *22*(5), 3535–3552. https://doi.org/10.5194/acp-22-3535-2022

Casadevall, T. J. (1994). The 1989–1990 eruption of Redoubt Volcano, Alaska: Impacts on aircraft operations. *Journal of Volcanology and Geothermal Research*, *62*(1), 301–316. https://doi.org/10.1016/0377-0273(94)90038-8

Clarisse, L., & Prata, F. (2016). Chapter 11—Infrared Sounding of Volcanic Ash. In S. Mackie, K. Cashman, H. Ricketts, A. Rust, & M. Watson (Eds.), *Volcanic Ash* (pp. 189–215). Elsevier. https://doi.org/10.1016/B978-0-08-100405-0.00017-3

Corradini, S., Merucci, L., & Prata, A. J. (2009). Retrieval of SO_2 from thermal infrared satellite measurements: Correction procedures for the effects of volcanic ash. *Atmospheric Measurement Techniques*, *2*(1), 177–191. https://doi.org/10.5194/amt-2-177-2009

Corradini, S., Spinetti, C., Carboni, E., Tirelli, C., Buongiorno, M. F., Pugnaghi, S., & Gangale, G. (2008). Mt. Etna tropospheric ash retrieval and sensitivity analysis using Moderate Resolution Imaging Spectroradiometer measurements. *Journal of Applied Remote Sensing*, *2*(1), 023550. https://doi.org/10.1117/1.3046674

Cox C., Polehampton E., & Smith D. (2021). *Sentinel-3 SLSTR Level-1 Algorithm and Theoretical Basis Document*, S3-TN-RAL-SL-032.

ha formattato: Italiano (Italia)

Formattato: Normale, Rientro: Sinistro: 0", Sporgente 0.49"

ha formattato: Italiano (Italia)

Formattato: Normale, Rientro: Sinistro: 0", Sporgente 0.49"

Craig, H., Wilson, T., Stewart, C., Outes, V., Villarosa, G., & Baxter, P. (2016). Impacts to agriculture and critical infrastructure in Argentina after ashfall from the 2011 eruption of the Cordón Caulle volcanic complex: An assessment of published damage and function thresholds. *Journal of Applied Volcanology*, *5*(1), 7. https://doi.org/10.1186/s13617-016-0046-1

Delmelle, P., Stix, J., Baxter, P., Garcia-Alvarez, J., & Barquero, J. (2002). Atmospheric dispersion, environmental effects and potential health hazard associated with the low-altitude gas plume of Masaya volcano, Nicaragua. *Bulletin of Volcanology*, *64*(6), 423–434. https://doi.org/10.1007/s00445-002-0221-6

Di Noia, A., & Hasekamp, O. P. (2018). Neural Networks and Support Vector Machines and Their Application to Aerosol and Cloud Remote Sensing: A Review. In A. Kokhanovsky (Ed.), *Springer Series in Light Scattering: Volume 1: Multiple Light Scattering, Radiative Transfer and Remote Sensing* (pp. 279–329). Springer International Publishing. https://doi.org/10.1007/978-3-319-70796-9_4

Fawcett, T. (2006). An introduction to ROC analysis. *Pattern Recognition Letters*, *27*(8), 861–874. https://doi.org/10.1016/j.patrec.2005.10.010

Francis, P. N., Cooke, M. C., & Saunders, R. W. (2012). Retrieval of physical properties of volcanic ash using Meteosat: A case study from the 2010 Eyjafjallajökull eruption. *Journal of Geophysical Research: Atmospheres*, *117*(D20). https://doi.org/10.1029/2011JD016788

Gardner, M. W., & Dorling, S. R. (1998). Artificial neural networks (the multilayer perceptron)—A review of applications in the atmospheric sciences. *Atmospheric Environment*, *32*(14), 2627–2636. https://doi.org/10.1016/S1352-2310(97)00447-0

Glaze, L. S., Baloga, S. M., & Wilson, L. (1997). Transport of atmospheric water vapor by volcanic eruption columns. *Journal of Geophysical Research: Atmospheres*, *102*(D5), 6099–6108. https://doi.org/10.1029/96JD03125

Gorkavyi, N., Krotkov, N., Li, C., Lait, L., Colarco, P., Carn, S., DeLand, M., Newman, P., Schoeberl, M., Taha, G., Torres, O., Vasilkov, A., & Joiner, J. (2021). Tracking aerosols and SO_2 clouds from the Raikoke eruption: 3D view from satellite observations. *Atmospheric Measurement Techniques*, *14*(12), 7545–7563. https://doi.org/10.5194/amt-14-7545-2021

ha formattato: Inglese (Stati Uniti)

Gray, T. M., & Bennartz, R. (2015). Automatic volcanic ash detection from MODIS observations using a back-propagation neural network. *Atmospheric Measurement Techniques*, *8*(12), 5089–5097. https://doi.org/10.5194/amt-8-5089-2015

Haywood, J., & Boucher, O. (2000). Estimates of the direct and indirect radiative forcing due to tropospheric aerosols: A review. *Reviews of Geophysics*, *38*(4), 513–543. https://doi.org/10.1029/1999RG000078

Horwell, C. J., & Baxter, P. J. (2006). The respiratory health hazards of volcanic ash: A review for volcanic risk mitigation. *Bulletin of Volcanology*, *69*(1), 1–24. https://doi.org/10.1007/s00445-006-0052-y

Horwell, C. J., Baxter, P. J., Hillman, S. E., Calkins, J. A., Damby, D. E., Delmelle, P., Donaldson, K., Dunster, C., Fubini, B., Kelly, F. J., Le Blond, J. S., Livi, K. J. T., Murphy, F., Nattrass, C., Sweeney, S., Tetley, T. D., Thordarson, T., & Tomatis, M. (2013). Physicochemical and toxicological profiling of ash from the 2010 and 2011 eruptions of Eyjafjallajökull and Grímsvötn volcanoes, Iceland using a rapid respiratory hazard assessment protocol. *Environmental Research*, *127*, 63–73. https://doi.org/10.1016/j.envres.2013.08.011

Mather, T. A., Pyle, D. M., & Oppenheimer, C. (2003). Tropospheric volcanic aerosol. In A. Robock & C. Oppenheimer (Eds.), *Geophysical Monograph Series* (Vol. 139, pp. 189–212). American Geophysical Union. https://doi.org/10.1029/139GM12

McKee, K., Smith, C. M., Reath, K., Snee, E., Maher, S., Matoza, R. S., Carn, S., Mastin, L., Anderson, K., Damby, D., Roman, D. C., Degterev, A., Rybin, A., Chibisova, M., Assink, J. D., de Negri Leiva, R., & Perttu, A. (2021). Evaluating the state-of-the-art in remote volcanic eruption characterization Part I: Raikoke volcano, Kuril Islands. *Journal of Volcanology and Geothermal Research*, *419*, 107354. https://doi.org/10.1016/j.jvolgeores.2021.107354

Menzel, W. P., Frey, R. A., & Baum, B. A. (2015~~n.d.~~). Cloud top properties and cloud phase algorithm theoretical basis document. 73.

Millán, L., Santee, M. L., Lambert, A., Livesey, N. J., Werner, F., Schwartz, M. J., Pumphrey, H. C., Manney, G. L., Wang, Y., Su, H., Wu, L., Read, W. G., & Froidevaux, L. (2022). The Hunga Tonga-Hunga Ha'apai Hydration of the Stratosphere. *Geophysical Research Letters*, *49*(13), e2022GL099381. https://doi.org/10.1029/2022GL099381

Murcray, D. G., Murcray, F. J., Barker, D. B., & Mastenbrook, H. J. (1981). Changes in Stratospheric Water Vapor Associated with the Mount St. Helens Eruption. *Science*, *211*(4484), 823–824. https://doi.org/10.1126/science.211.4484.823

Formattato: Normale, Rientro: Sinistro: 0", Sporgente 0.49"

ha formattato: Tedesco (Germania)

Muser, L. O., Hoshyaripour, G. A., Bruckert, J., Horváth, Á., Malinina, E., Wallis, S., Prata, F. J., Rozanov, A., von Savigny, C., Vogel, H., & Vogel, B. (2020). Particle aging and aerosol–radiation interaction affect volcanic plume dispersion: Evidence from the Raikoke 2019 eruption. *Atmospheric Chemistry and Physics*, *20*(23), 15015–15036. https://doi.org/10.5194/acp-20-15015-2020

Nishihama M., Blanchette J., Fleig A., Freeze M., Patt F. & Wolfe R. (1998). *MODIS Level 1A Earth Location: Algorithm Theoretical Basis Document Version 3.0.*

Oppenheimer, C., Scaillet, B., & Martin, R. S. (2011). Sulfur Degassing From Volcanoes: Source Conditions, Surveillance, Plume Chemistry and Earth System Impacts. *Reviews in Mineralogy and Geochemistry*, *73*(1), 363–421. https://doi.org/10.2138/rmg.2011.73.13

Pavolonis, M. J. (2010). Advances in Extracting Cloud Composition Information from Spaceborne Infrared Radiances—A Robust Alternative to Brightness Temperatures. Part I: Theory. *Journal of Applied Meteorology and Climatology*, *49*(9), 1992–2012. https://doi.org/10.1175/2010JAMC2433.1

Pavolonis, M., & Sieglaff, J. (2012). *GOES-R Advanced Baseline Imager (ABI) Algorithm Theoretical Basis Document For Volcanic Ash (Detection and Height)*. 71.

Picchiani, M., Chini, M., Corradini, S., Merucci, L., Piscini, A., & Frate, F. D. (2014). Neural network multispectral satellite images classification of volcanic ash plumes in a cloudy scenario. *Annals of Geophysics*, *57*. https://doi.org/10.4401/ag-6638

Picchiani, M., Chini, M., Corradini, S., Merucci, L., Sellitto, P., Del Frate, F., & Stramondo, S. (2011). Volcanic ash detection and retrievals using MODIS data by means of neural networks. *Atmospheric Measurement Techniques*, *4*(12), 2619–2631. https://doi.org/10.5194/amt-4-2619-2011

Picchiani, M., Del Frate, F., & Sist, M. (2018). A Neural Network Sea-Ice Cloud Classification Algorithm for Copernicus Sentinel-3 Sea and Land Surface Temperature Radiometer. *IGARSS 2018 - 2018 IEEE International Geoscience and Remote Sensing Symposium*, 3015–3018. https://doi.org/10.1109/IGARSS.2018.8517857

Piscini, A., Carboni, E., Del Frate, F., & Grainger, R. G. (2014). Simultaneous retrieval of volcanic sulphur dioxide and plume height from hyperspectral data using artificial neural networks. *Geophysical Journal International*, *198*(2), 697–709. https://doi.org/10.1093/gji/ggu152

Polehampton E., Cox C., Smith D., Ghent D., Wooster M., Xu W., Bruniquel J. & Dransfeld S. (2021). *Copernicus Sentinel-3 SLSTR Land User Handbook*, 3MPC.ACR.HBK.002.

Prata, A. J. (1989a). Infrared radiative transfer calculations for volcanic ash clouds. *Geophysical Research Letters*, *16*(11), 1293–1296. https://doi.org/10.1029/GL016i011p01293

Prata, A. J. (1989b). Observations of volcanic ash clouds in the 10-12 µm window using AVHRR/2 data. *International Journal of Remote Sensing*, *10*(4–5), 751–761. https://doi.org/10.1080/01431168908903916

Prata, A. J., & Grant, I. F. (2001). *Determination of mass loadings and plume heights of volcanic ash clouds from satellite data*. https://publications.csiro.au/rpr/pub?list=BRO&pid=procite:d76866c5-98ff-40a4-a7cb-80c5fad7f6da

Prata, A. T., Grainger, R. G., Taylor, I. A., Povey, A. C., Proud, S. R., & Poulsen, C. A. (2022). Uncertainty-bounded estimates of ash cloud properties using the ORAC algorithm: Application to the 2019 Raikoke eruption. *Atmospheric Measurement Techniques Discussions*, 1–35. https://doi.org/10.5194/amt-2022-166

Prata, F., Bluth, G., Rose, B., Schneider, D., & Tupper, A. (2001). Comments on "Failures in detecting volcanic ash from a satellite-based technique." *Remote Sensing of Environment*, *78*(3), 341–346. https://doi.org/10.1016/S0034-4257(01)00231-0

Rose, W. I., Delene, D. J., Schneider, D. J., Bluth, G. J. S., Krueger, A. J., Sprod, I., McKee, C., Davies, H. L., & Ernst, G. G. J. (1995). Ice in the 1994 Rabaul eruption cloud: Implications for volcano hazard and atmospheric effects. *Nature*, *375*(6531), 477–479. https://doi.org/10.1038/375477a0

Shinohara, H. (2008). Excess degassing from volcanoes and its role on eruptive and intrusive activity. *Reviews of Geophysics*, *46*(4). https://doi.org/10.1029/2007RG000244

Solomon, S., Daniel, J. S., Neely, R. R., Vernier, J.-P., Dutton, E. G., & Thomason, L. W. (2011). The Persistently Variable "Background" Stratospheric Aerosol Layer and Global Climate Change. *Science*, *333*(6044), 866–870. https://doi.org/10.1126/science.1206027

Toller G. N., Isaacman, A., Kuyper J., Geng X. & Xiong J. (2017). *MODIS Level 1B Product User's Guide*. 62.

Vermote, E. F. & Vermeulen A. (1999). *MODIS Algorithm Technical Background Document, ATMOSPHERIC CORRECTION ALGORITHM: SPECTRAL REFLECTANCES (MOD09)*.

Vogl, T. P., Mangis, J. K., Rigler, A. K., Zink, W. T., & Alkon, D. L. (1988). Accelerating the convergence of the back-propagation method. Biological Cybernetics, 59(4), 257–263. https://doi.org/10.1007/BF00332914

ha formattato: Tipo di carattere: Corsivo

Formattato: Normale, Rientro: Sinistro: 0", Sporgente 0.49"

ha formattato: Inglese (Regno Unito)

Formattato: Rientro: Sinistro: 0", Sporgente 0.49"

ha formattato: Inglese (Regno Unito)

ha formattato: Inglese (Regno Unito)

ha formattato: Tipo di carattere: Corsivo

Xu, J., Li, D., Bai, Z., Tao, M., & Bian, J. (2022). Large Amounts of Water Vapor Were Injected into the Stratosphere by the Hunga Tonga–Hunga Ha'apai Volcano Eruption. *Atmosphere*, *13*(6), 912. https://doi.org/10.3390/atmos13060912